ChemComm

COMMUNICATION

View Article Online
View Journal

Cite this: DOI: 10.1039/d5cc06351e

Received 8th November 2025,
Accepted 6th February 2026

DOI: 10.1039/d5cc06351e

rsc.li/chemcomm

Metal-hydride-free one-pot synthesis of InSb/InP core/shell quantum dots for light-emitting diodes

Cong Zhang,[ab] Hiroyuki Yamada,[a] Daniel Limouchi,[ab] Kazuhiro Nemoto *[a] and Naoto Shirahata *[abc]

A one-pot synthesis of InSb/InP core–shell quantum dots (QDs) using aminopnictogen precursors enhanced the photoluminescence quantum yield (PLQY) from 0.8% to 7.0% compared to InSb cores. For the first time, InSb/InP QD-based QLEDs exhibiting NIR-SWIR electroluminescence were demonstrated.

Near-infrared (NIR) and short-wavelength infrared (SWIR) emissive quantum dots (QDs) have attracted considerable attention in recent years for applications such as photodetection,[1,2] QD light-emitting diodes (QLEDs),[3–6] and bioimaging,[7] owing to their tunable narrow bandgaps and narrow emission spectra.[8] Among them, mercury and lead-based QDs exhibit excellent optoelectrical performance.[9–13] Toxicity concerns have however led to the inclusion of these materials under the RoHS directive, severely restricting their practical applications. In contrast, the group III–V compound InSb has attracted significant interest in recent years as a promising, RoHS-compliant candidate for NIR and SWIR applications.[14]

Since Evans and co-workers first reported the synthesis of InSb QDs using tris(trimethylsilyl)antimony (TMS-Sb) in 2008,[15] extensive efforts have been devoted to developing synthetic methods employing less reactive precursors to achieve better control over crystal growth.[1,15–24] However, in all these reported studies, the reducing agents used have almost exclusively been highly reactive metal hydrides, such as Super-hydrides[1,15–23] and Alane-complexes.[24] There remains a clear lack of research into InSb QD syntheses utilizing low-reactivity reducing agents. The main challenge arises from the requirement that both In and Sb precursors must be reduced to their metallic states prior to the zero-valent reaction that forms InSb.[14,21] Due to their different oxidation potentials, weak reducing agents cannot simultaneously and proportionally reduce both In and Sb precursors to their metallic states, often resulting in the excessive formation of metallic by-products. Consequently, only highly reactive, though less controllable, metal hydrides have been adopted as reducing agents in previous studies.

In our previous work,[25] we explored an alternative synthetic strategy by employing the less reactive, metal-hydride-free compound tris(dimethylamino)phosphine ($P(NMe_2)_3$) as a reducing agent for the synthesis of InSb QDs. This compound has also been utilized as a mild reducing agent in recently reported syntheses of other III–V QDs, including InP,[26] InAs[27] and InSb.[25] In the synthesis of InP QDs,[26] $P(NMe_2)_3$ first undergoes an amine-exchange reaction with oleylamine (OLA) to form $P(NHR)_3$ species. This intermediate subsequently undergoes a disproportionation reaction, in which it simultaneously acts as both the phosphorus precursor and the reducing agent, leading to the formation of InP. In contrast, during InAs[27] and InSb[25] QD synthesis, the $P(NHR)_3$ primarily acts to reduce the arsenic and antimony precursors, enabling the formation of InAs and InSb QDs. This approach demonstrated that a low-reactivity reductant can enable the controlled growth of high-quality InSb QDs exhibiting distinct and sharp excitonic peaks in their ultraviolet-visible-NIR (UV-vis-NIR) absorption spectra, while effectively suppressing the formation of metallic by-products. Nevertheless, their photoluminescence quantum yield (PLQY) remained below 1%, similar to most reported colloidal InSb QDs,[1,15–24] indicating that substantial improvements are still required for practical applications, particularly in QLED devices. For other III–V group QDs, the formation of core/shell structures is the most effective strategy for enhancing PLQY.[28,29] However, the large lattice constant (6.48 Å) of InSb leads to significant lattice mismatch with conventional III–V shell materials (like ZnSe, ZnS), thereby increasing the difficulty of core/shell synthesis. To date, three research groups have successfully synthesized InSb core/shell QDs, all employing a stepwise core–shell synthesis approach. In Talapin's report,[23] InSb/CdS, InSb/CdSe and InSb/ZnTe core/shell QDs were also explored while Kim and his collaborators[30] synthesized InSb/InAs core/shell QDs. Both reports did not include PLQY measurement results.

[a] Research Center for Materials Nanoarchitectonics (MANA), National Institute for Materials Science (NIMS), 1-1 Namiki, Tsukuba 305-0044, Japan. E-mail: nemoto.kazuhiro@nims.go.jp, shirahata.naoto@nims.go.jp
[b] Graduate School of Chemical Sciences and Engineering, Hokkaido University, Sapporo 060-0814, Japan
[c] Department of Physics, Chuo University, 1-13-27 Kasuga, Bunkyo, Tokyo 112-8551, Japan

Konstantatos and co-workers reported the synthesis of InSb/InP core/shell QDs using tris(trimethylsilyl)phosphine (TMS-P) as the phosphorus precursor for shell formation, achieving a PLQY of 3.7%,[31] which was recently further improved to 10%.[32] This demonstrates the great potential of InP as a shell material for significantly enhancing the PLQY of InSb QDs. Such progress represents a major breakthrough and provides strong impetus for further development of InSb core/shell QDs. In this work, instead of employing a metal hydride as the reducing agent and TMS-P as the phosphorus precursor for shell growth, we adopted a one-pot synthesis approach in which $P(NMe_2)_3$ served simultaneously as both the reducing agent and the phosphorus source. We successfully synthesized InSb/InP core/shell QDs exhibiting PLQY enhancements from 0.8% to 7.0% at 1.23 eV (1000 nm) and from 0.4% to 3.0% at 0.97 eV (1270 nm). The resulting core/shell QDs exhibit narrow size distributions, characterized by a photoluminescence (PL) full-width at half-maximum (FWHM) of 0.12 eV, comparable to the state-of-the-art record.[32] Using these InSb/InP QDs, we fabricated QLED devices showing electroluminescence (EL) in the NIR and SWIR regions.

As illustrated in the schematic in Fig. 1a, the InSb/InP core/shell QDs were synthesized *via* a one-pot approach (see experimental section, SI for more details). Initially, InSb core QDs were synthesized *via* a hot-injection method using indium laurate ($InLA_3$) as the indium precursor, octadecene (ODE) as the solvent, antimony chloride ($SbCl_3$) as the Sb source, and $P(NMe_2)_3$ as the reducing agent. In the oleylamine (OLA)-containing reaction environment, $P(NMe_2)_3$ stock readily undergoes an amine-exchange reaction with OLA to form $P(NHR)_3$ and its derivatives, which serve as the actual reactive phosphorus-containing intermediates. The formation of $P(NHR)_3$ is confirmed by ^{31}P-NMR spectroscopy of the $P(NMe_2)_3$ precursor solution, which exhibits characteristic resonance features attributable to $P(NHR)_3$ and its derivatives (Fig. S1), in good agreement with previous reports.[26] Subsequently, the precursors for InP shell growth—$InLA_3$ and $P(NMe_2)_3$ stock—were hot-injected directly into the as-synthesized InSb crude solution, promoting the epitaxial growth of an InP shell on the InSb cores and leading to the formation of InSb/InP core/shell QDs. Following centrifugation (Scheme S1), different sizes of QDs could be separated (see Fig. S2 and S3). Fig. 1b and Fig. S2c and d show transmission electron microscope (TEM) images and high-angle annular dark field scanning TEM (HAADF-STEM) images comparing the large size InSb core (QDs-BC) QDs before and after core/shell construction (QDs-BCS). As shown in Fig. S2 and S3, the InSb core QDs exhibit uniform morphology, with an average diameter of 4.0 nm, a narrow size distribution (σ =12%), and nearly spherical shape. After the growth of the InP shell, the InSb/InP core/shell QDs remain spherical and retain a uniform size, with an average diameter of 5.0 nm and a narrow distribution of σ =11% (see Fig. S3). The increase in particle size after shell construction serves as evidence for the core/shell formation. Powder X-ray diffraction (PXRD) patterns in Fig. 1c show that the synthesized cores exhibit high crystallinity, with distinct diffraction reflections corresponding to the (111), (220) and (331) planes, consistent with literature data (ICSD #162196). After shell formation, the PXRD reflection of the core/shell QDs shifts slightly toward the characteristic diffraction positions of the InP (ICSD #41443) shell. This behavior is consistent with the observed trend in core/shell nanostructures, where increasing shell thickness leads to a gradual shift of the diffraction reflection from the core toward the shell positions.[30] Such a reflection shift thus supports the formation of the InSb/InP core/shell structure. For the extended X-ray absorption fine structure (EXAFS) measurements, as shown in Fig. 1d, a peak around 2.0 Å corresponding to In–P bonding could be observed in the FT-EXAFS spectrum of indium in InP, while that of InSb shows a sharp peak near 2.5 Å corresponding to In–Sb bonding. In contrast, the spectrum of the InSb/InP QDs reveals the coexistence of both In–Sb and In–P coordination environments. Fig. S4 shows the HRTEM image of the InSb/InP QDs, in which clear lattice fringes are observed. The measured interplanar spacing ~1.93 Å corresponds well to the (311) plane of InSb (1.92 Å). This result indicates that the QDs adopt a core/shell structure rather than an alloyed structure. The InSb core is clearly resolved, while the InP shell is too thin to be directly distinguished in the HRTEM image.

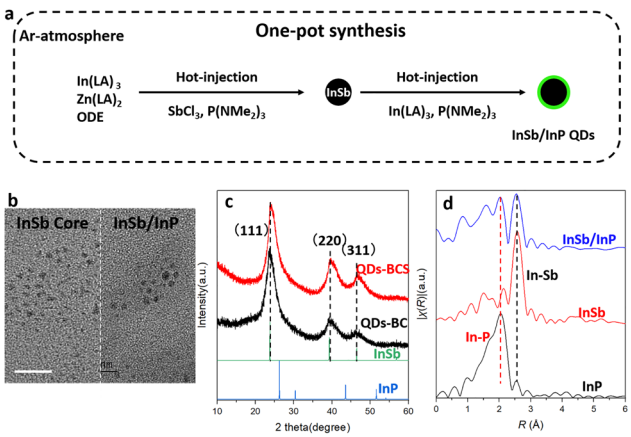

Fig. 1 Schematic illustration (a) of InSb core–shell QD one-pot synthesis; TEM images (b) for InSb QDs before and after core–shell formation, where the scale bar is 20 nm; PXRD results (c) for QDs-BC (black), QDs-BCS (red), Bulk InSb (green) and InP (blue) from the ICSD database (InSb: ICSD #162196 and InP: ICSD #41443); (d) FT-EXAFS results for InP (black), InSb (red) and InSb/InP (blue).

Both the as-synthesized core and core/shell QDs could be size-selected into small and large fractions by centrifugation, resulting in four distinct samples: QDs-BC, QDs-BCS, small InSb core QDs (QDs-SC), and small InSb/InP core/shell QDs (QDs-SCS). The UV-vis-NIR absorption and PL spectra of the QDs-BCS are summarized in Fig. 2a. Distinct and sharp excitonic absorption peaks are observed in both the QDs-BC and QDs-BCS (Fig. 2a and Fig. S5c), indicating a narrow size distribution among the nanocrystals and pronounced exciton confinement effects. The strong confinement implies a low density of structural or surface defects within the QDs.[30] The excitonic absorption peak of QDs-BC is located at 1.13 eV (~1100 nm). After shell growth, the peak observed for QDs-BCS becomes sharper (peak-to-valley ratio improved from 1.127 to 1.246) and exhibits a slight red-shift to 1.11 eV (~1120 nm). Regarding the PL spectra (Fig. S5d), both QDs-BC and QDs-BCS

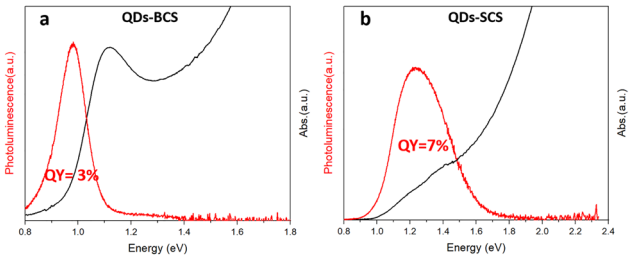

Fig. 2 The UV-vis-NIR absorption spectrum (black) and PL spectrum (red) of QDs-SCS (a) and QDs-BCS (b).

display approximately Gaussian emission profiles. The PL peak of QDs-BC appears at 1.03 eV (~1207 nm) with FWHM = 0.14 eV and PLQY = 0.4%. After the formation of the core/shell structure, the PL peak of the QDs-BCS red-shifts to 0.98 eV (~1270 nm) with a narrower FWHM of 0.12 eV—comparable to the state-of-the-art record among InSb QDs[31]—and the PLQY increases to 3.0%. In contrast, the smaller-sized QDs (QDs-SC and QDs-SCS) exhibit weaker confinement signatures. As shown in Fig. 2b, the absorption shoulder of the QDs-SCS is not well defined, presenting only a weak slope around 1.37 eV (~900 nm), similar to the core QDs-SC (Fig. S5a). The PL spectrum of the QDs-SCS slightly red-shifts to 1.23 eV (~1000 nm) accompanied by a remarkable enhancement of PLQY from 0.8% to 7%, compared to the core QDs-SC (Fig. S5b). The broad absorption shoulders and PL linewidths of both QDs-SC and QDs-SCS are attributed to their relatively broad size distributions. As shown in Fig. S3, the average diameter of the QDs-SC is approximately 3.6 nm with a size dispersion of about 20%. The same broad size distribution leads to a correspondingly wide PL bandwidth exceeding 300 meV. The correlation between the energy bandgap and particle size of the synthesized InSb QDs, together with the reported theoretically calculated values obtained using the tight-binding model,[22] is presented in Fig. S6. The experimentally measured bandgap values are slightly higher than the theoretical predictions, yet the overall trend exhibits excellent consistency with the calculated results. The pronounced increase in PLQY provides compelling evidence for the successful formation of the core/shell structure. As summarized in Table S1, the PLQY of previously reported InSb QDs without surface passivation is typically below 1%, whereas a clear enhancement is observed after core/shell formation, consistent with our results. Furthermore, the red-shifts observed in both the absorption and PL peaks support the formation of a core/shell architecture rather than an alloyed structure. In an alloyed system incorporating the wider-bandgap InP component, a blue-shift would be expected. Notably, similar red-shift behavior has also been reported in previously studied InSb/InP core/shell QDs, further corroborating this interpretation. The observed bathochromic shifts therefore indicate effective shell growth and surface passivation instead of compositional alloying.

We fabricated QLEDs using the QDs-SCS core/shell QDs as the emissive layer in an inverted device architecture, as illustrated in Fig. 3a. The cross-sectional scanning electron microscopy (SEM) image in Fig. 3a reveals a smooth interface between each layer and the thicknesses of the individual layers are as follows: ITO (thickness is 130 nm, coated on glass substrate)/ZnO (80 nm)/InSb QDs (16 nm)/TCTA (35 nm)/MoO_3 (14 nm)/Al (200 nm). In contrast to conventional QLEDs, electrons and holes are injected from the ITO cathode and the Al anode, as is shown in the flat energy band diagram in Fig. 3b. The highest occupied molecular orbital (HOMO) and lowest unoccupied molecular orbital (LUMO) of the InSb QD layer were determined using ultraviolet photoelectron spectroscopy (UPS) (see Fig. S7) and the bandgap energy estimated from the PL spectrum. The energy levels of the other layers were previously reported.[33] The device current density–voltage (J–V) and optical power density–voltage (L–V) characteristics of the device are shown in Fig. 3c. The LED exhibits a turn-on voltage of 3.3 V, defined as the voltage at which the optical power density exceeds 0.1 nW cm^{-2}. Both the current density and the optical power density increase monotonically with increasing applied voltage. At an operating voltage of 7 V, the device reaches a current density of 140 mA cm^{-2} and an optical power density of 3.45 μW cm^{-2}. The external quantum efficiency (EQE)–voltage characteristics are presented in Fig. S8. The maximum EQE value is 0.003% at 6 V, after which it gradually decreases at higher voltages. To evaluate the reproducibility of the device performance, a total of 11 devices were fabricated. Their maximum EQE values fell within the range of 0.0028% to 0.0038% (see Fig. S9). The relatively low EQE is attributed primarily to the limited PLQY of the QDs and the use of long-chain ligands, which hinder efficient charge injection and transport. Increasing the PLQY of the QDs by optimizing shell materials (such as InAs) and implementing more effective ligand exchange

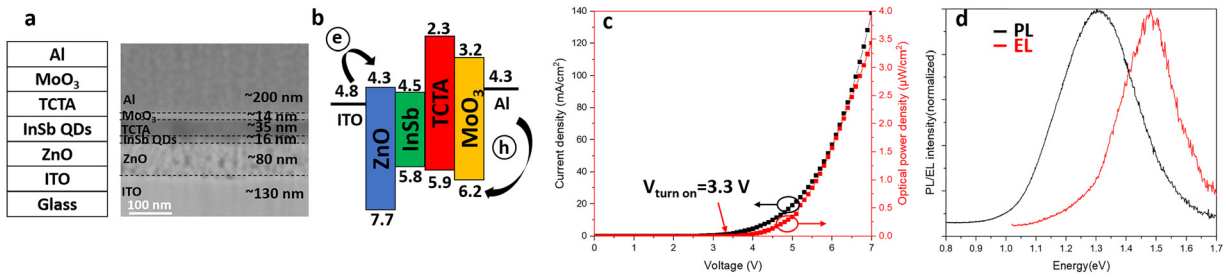

Fig. 3 Illustration and cross-section SEM image of the QLED devices (a); flat energy band diagram (b) of the QLED devices; J–V–L characteristics (c) of the QDs-SCS-based QLED; EL spectrum of the QDs-SCS based QLED at 7 V and PL spectrum of the QDs used in the fabrication (d).

strategies is expected to improve LED performance. The electroluminescence (EL) spectrum of the device measured at 7 V as well as the PL spectrum of the QDs used for device fabrication are shown in Fig. 3d. The EL peak appears at approximately 1.45 eV (850 nm) and closely resembles the PL spectral profile, albeit with a noticeable blue-shift. As shown in Fig. S10, only weak EL emission is observed at a bias of 4 V, with the emission peak centered at ~900 nm. Upon increasing the driving voltage to 7 V, the EL intensity increases significantly, accompanied by a further blue-shift of the emission peak to 850 nm. This progressive blue-shift with increasing bias is most likely attributable to free-carrier screening and/or band-filling effects under high current injection, as commonly reported in QD-based LEDs. In contrast, Joule heating typically induces a red-shift in the EL spectra;[34] thermal effects are therefore not considered to be the dominant factor governing the observed spectral evolution. The operational stability of the LED devices under ambient conditions was also evaluated. As shown in Fig. S11, when operated at a constant bias of 5 V, the devices exhibit an EL half-lifetime of 6300 s, demonstrating reasonable short-term stability without encapsulation. QLED devices were also fabricated using the QDs-BCS samples. As shown in Fig. S12, under a bias of 10 V, pronounced EL emission was observed, with the EL peak centered at 1170 nm, corresponding to the SWIR region. Similar to the QDs-SCS devices, the EL spectrum exhibits a pronounced blue-shift relative to the corresponding PL spectrum, which is centered at 1270 nm.

In summary, this work demonstrates the one-pot synthesis of InSb/InP core/shell QDs using $P(NMe_2)_3$ as both the reducing agent and the phosphorus precursor. Compared to the InSb cores, the core/shell QDs exhibit markedly enhanced PLQY values of up to 7.0% at 1000 nm and 3.0% at 1270 nm, on par with the best results reported to date. The formation of the core/shell structure is corroborated by analytical observations. QLEDs fabricated using these QDs exhibit EL in both the NIR (850 nm, 1.45 eV) and SWIR (1170 nm, 1.06 eV) regions, with a determined EQE of 0.003% at 6 V and 850 nm. Although the device performance is still far below the levels required for practical applications in commercial devices, this study highlights the strong efficacy and considerable potential of $P(NMe_2)_3$ for use in core/shell syntheses, and provides a valuable strategy for the fabrication of InSb-based QLED devices.

We are very grateful for a part of this work was supported by ''Advanced Research Infrastructure for Materials and Nanotechnology in Japan (ARIM)'' of the Ministry of Education, Culture, Sports, Science and Technology (MEXT): Proposal Number JPMXP1225NM5200. We thank to the financial support by WPI program, JSPS KAKENHI (Grant No. 24K01462, 24K21720 and 23KJ2166) and Hosokawa Powder Technology Foundation (Grant Number HPTF24111).

Conflicts of interest

There are no conflicts to declare.

Data availability

The data supporting the findings of this study are available from the corresponding author upon reasonable request.

Supplementary information (SI): experimental, centrifugation process, STEM, PL spectra, absorption spectra, and EL spectra. See DOI: https://doi.org/10.1039/d5cc06351e.

References

1 S. Chatterjee, K. Nemoto, B. Ghosh, H.-T. Sun and N. Shirahata, *ACS Appl. Nano Mater.*, 2023, **6**, 15540–15550.
2 C. Li, W. Huang, L. Gao, H. Wang, L. Hu, T. Chen and H. Zhang, *Nanoscale*, 2020, **12**, 2201–2227.
3 J. Watanabe, H. Yamada, H.-T. Sun, T. Moronaga, Y. Ishii and N. Shirahata, *ACS Appl. Nano Mater.*, 2021, **4**, 11651–11660.
4 M. Vasilopoulou, A. Fakharuddin, F. P. García de Arquer, D. G. Georgiadou, H. Kim, A. R. B. Mohd Yusoff, F. Gao, M. K. Nazeeruddin, H. J. Bolink and E. H. Sargent, *Nat. Photonics*, 2021, **15**, 656–669.
5 J. Lim, W. K. Bae, D. Lee, M. K. Nam, J. Jung, C. Lee, K. Char and S. Lee, *Chem. Mater.*, 2011, **23**, 4459–4463.
6 X. Yang, S. M. H. Qaid, B. Wang, W. Cai, Q. Qian and Z. Zang, *Inorg. Chem.*, 2023, **62**, 18591–18598.
7 S. Chinnathambi and N. Shirahata, *Sci. Technol. Adv. Mater.*, 2019, **20**, 337–355.
8 J. A. del Alamo, *Nature*, 2011, **479**, 317–323.
9 S. Zhao, Y. Zhang and Z. Zang, *Chem. Commun.*, 2020, **56**, 5811–5814.
10 C. Gréboval, A. Chu, N. Goubet, C. Livache, S. Ithurria and E. Lhuillier, *Chem. Rev.*, 2021, **121**, 3627–3700.
11 C. Livache, B. Martinez, N. Goubet, J. Ramade and E. Lhuillier, *Front. Chem.*, 2018, **6**, 2018.
12 S. B. Hafiz, M. Scimeca, A. Sahu and D.-K. Ko, *Nano Convergence*, 2019, **6**, 7.
13 Y. Tian, H. Luo, M. Chen, C. Li, S. V. Kershaw, R. Zhang and A. L. Rogach, *Nanoscale*, 2023, **15**, 6476–6504.
14 H. Xie, C. Zhang, R. Yang, J. Xu, Y. Pan and X. Yin, *Laser Photon. Rev.*, 2025, **19**, 2401204.
15 C. M. Evans, S. L. Castro, J. J. Worman and R. P. Raffaelle, *Chem. Mater.*, 2008, **20**, 5727–5730.
16 S. Chatterjee, K. Nemoto, H.-T. Sun and N. Shirahata, *Nanoscale Horiz.*, 2024, **9**, 817–827.
17 M. Yarema and M. V. Kovalenko, *Chem. Mater.*, 2013, **25**, 1788–1792.
18 S. Tamang, K. Kim, H. Choi, Y. Kim and S. Jeong, *Dalton Trans.*, 2015, **44**, 16923–16928.
19 M. He, Z. Xu, S.-W. Zhang, M. Zhang, C. Wu, B. Li, J. Li, L. Wang, S. Zhao, F. Kang and G. Wei, *Adv. Photon. Res.*, 2022, **3**, 2100305.
20 W. J. Mir, T. Sheikh, S. Nematulloev, P. Maity, K. E. Yorov, A.-H. Emwas, M. N. Hedhili, M. S. Khan, M. Abulikemu, O. F. Mohammed and O. M. Bakr, *Small*, 2024, **20**, 2306535.
21 Y. Zhang, P. Xia, B. Rehl, D. H. Parmar, D. Choi, M. Imran, Y. Chen, Y. Liu, M. Vafaie, C. Li, O. Atan, J. M. Pina, W. Paritmongkol, L. Levina, O. Voznyy, S. Hoogland and E. H. Sargent, *Angew. Chem., Int. Ed.*, 2024, **63**, e202316733.
22 S. Busatto, M. de Ruiter, J. T. B. H. Jastrzebski, W. Albrecht, V. Pinchetti, S. Brovelli, S. Bals, M.-E. Moret and C. de Mello Donega, *ACS Nano*, 2020, **14**, 13146–13160.
23 W. Liu, A. Y. Chang, R. D. Schaller and D. V. Talapin, *J. Am. Chem. Soc.*, 2012, **134**, 20258–20261.
24 Muhammad, D. Choi, D. H. Parmar, B. Rehl, Y. Zhang, O. Atan, G. Kim, P. Xia, J. M. Pina, M. Li, Y. Liu, O. Voznyy, S. Hoogland and E. H. Sargent, *Adv. Mater.*, 2023, **35**, 2306147.
25 C. Z. Kazuhiro Nemoto, H.-T. Sun and N. Shirahata, *ChemRxiv*, preprint, 2025, DOI: 10.26434/chemrxiv-2025-x9c2k.
26 A. Buffard, S. Dreyfuss, B. Nadal, H. Heuclin, X. Xu, G. Patriarche, N. Mézailles and B. Dubertret, *Chem. Mater.*, 2016, **28**, 5925–5934.
27 R. Tietze, R. Panzer, T. Starzynski, C. Guhrenz, F. Frenzel, C. Würth, U. Resch-Genger, J. J. Weigand and A. Eychmüller, *Part. Part. Syst. Charact.*, 2018, **35**, 1800175.
28 B. Chen, D. Li and F. Wang, *Small*, 2020, **16**, 2002454.

29 H. Li, W. Zhang, Y. Bian, T. K. Ahn, H. Shen and B. Ji, *Nano Lett.*, 2022, **22**, 4067–4073.
30 H. Seo, H. J. Eun, A. Y. Lee, H. K. Lee, J. H. Kim and S.-W. Kim, *Adv. Sci.*, 2024, **11**, 2306439.
31 L. Peng, Y. Wang, Y. Ren, Z. Wang, P. Cao and G. Konstantatos, *ACS Nano*, 2024, **18**, 5113–5121.
32 L. Peng, Y. Wang, C. Rodà, A. Malla, M. Dosil, D. Mandal and G. Konstantatos, *Adv. Sci.*, 2025, **12**, 2502775.
33 H. Yamada, T. Nagao and N. Shirahata, *Nanoscale Adv.*, 2025, **7**, 4837–4841.
34 Z. Gong, S. Jin, Y. Chen, J. McKendry, D. Massoubre, I. M. Watson, E. Gu and M. D. Dawson, *J. Appl. Phys.*, 2010, **107**, 013103.